Volume 9, Issue 2, 2020, 1049 - 1057 ISSN 2284-6808

Letters in Applied NanoBioScience

https://nanobioletters.com/

https://doi.org/10.33263/LIANBS92.10491057

Original Research Article Open Access Journal

Received: 15.04.2020 / Revised: 07.05.2020 / Accepted: 07.05.2020 / Published on-line: 10.05.2020

Comparison of the effect of magnetite (Fe_3O_4) iron oxide nanoparticles on melanoma cells and healthy cells: an *in vitro* study

Kurtulus Gokduman [1, *]

[1] Department of Biotechnology, Middle East Technical University, 06800 Ankara, Turkey; Institute of Biomedical Engineering, Bogazici University, Istanbul 34684, Turkey

*corresponding author e-mail address: ***k.gokduman@gmail.com*** | Scopus ID 25723120100

ABSTRACT

The aim of the current study is to investigate the anti-melanoma activity of bare magnetite (Fe3O4) iron oxide nanoparticles (MION) by comparing their effects on healthy cells. MION were synthesized, and characterized using Fourier transform infrared (FT-IR) spectroscopy, powder X-ray diffraction (XRD) and particle size analyzer; anti-melanoma activity of the nanoparticles (50-400 µg/ml) was investigated on melanoma cell lines (A375 and G361 cells) using normal human umbilical vein/vascular endothelium cell line (HUVEC) as control by focusing on intracellular reactive oxygen species (ROS) level, viability and apoptosis through caspase-3 activity. FT-IR, XRD and particle size analyses results have illustrated that the synthesized MION (45.36 ± 0.33 nm) have attractive characteristics for biomedical applications. The MION have induced highly significant ($p<0.01$) dose-dependent increases in ROS levels in normal and melanoma cells. In addition, cellular interaction assays have illustrated that the MION have an effect on selectively killing the melanoma cells (IC50 values for HUVEC, G361 and A375 cells after 24h-treatment are 549.37 ± 20.48, 219.93 ± 15.76 and 152.02 ± 7.34 µg/ml, respectively, and after 72h-treatment are 270.69 ± 13.35, 151.41 ±8.61 and 102.56 ± 6.64 µg/ml, respectively) by selectively targeting mitochondria in cancerous cells that induce ROS mediated caspase-3 activation and apoptosis (the lowest ($p<0.01$) apoptosis and caspase-3 activity rates were observed in HUVEC cells compared to A375 and G361 cells). Thus, for further investigations, the synthesized MION can be considered as a potent agent in melanoma treatment or in combination therapies for melanoma treatment.

Keywords: *Magnetite (Fe_3O_4) Iron Oxide Nanoparticles; Melanoma; A375; G361; HUVEC; ROS; Apoptosis; Caspase-3.*

1. INTRODUCTION

In the 21st century, cancer is expected to be the most important cause of death and to be the leading barrier to increasing life expectancy; 18.1 million new cancer cases and 9.6 million cancer deaths have been mentioned in 2018 estimates [1]. Melanoma is the sixth most frequently diagnosed cancer in humans and the most serious form of skin cancer causing most of the skin cancer-related deaths (80%); in terms of increased incidence over the past few years, no other solid or blood malignancy comes close to the incidence of melanoma; the main problem of melanoma treatment is the low response rate to conventional therapies [2-4]. Therefore, new strategies are required for the treatment of melanoma.

Nanotechnology represents a promising strategy for the development of new cancer treatments by protecting sensitive therapeutic agents from degradation, and by improving the bioavailability, the efficacy and the tolerability of drugs; especially, the number of studies covering nanomedicines as a potential therapy for melanoma has considerably increased over the last 5 years [4-7]. In this context, iron oxide nanoparticles are very promising candidates. Since, they possess unique physicochemical features such as ultrafine sizes and a large surface area to mass ratio [6, 8]; they are currently the only clinically approved metal oxide nanoparticles, besides they are the most commonly used superparamagnetic nanoparticles [8, 9]; they have a wide variety of biomedical applications [5, 6, 10], such as magnetic resonance imaging [11, 12, 13], targeted delivery of drugs [5, 14] or genes [15, 16], tissue engineering [17, 18], hyperthermia of cancer [19, 20], magnetic transfections [21, 22]; ferumoxytol (Feraheme), ferumoxides, ferucarbotran, ferumoxtran-10, ferristene and ferumoxsil are iron oxide nanoparticle-based magnetic resonance imaging contrast agents at current clinical trials [11, 12, 13].

On the other hand, usage of nanoparticles as anti-cancer agent is quite a new strategy; e.g., a recent study [23] reported potential therapeutic use of single-walled carbon nanotube, multi-walled carbon nanotube and maghemite iron oxide nanoparticles in the treatment of melanoma through reactive oxygen species (ROS) mediated mitochondrial targeting. Structure of magnetite (Fe_3O_4) nanoparticles contains Fe^{3+} in all the tetrahedral sites, and Fe^{3+} or Fe^{2+} in the octahedral sites; but structure of maghemite (Fe_2O_3) nanoparticles mostly contains Fe^{3+} in all the octahedral sites. Thus, the dissolution of magnetite nanoparticles releases Fe^{3+} or Fe^{2+} while the dissolution of maghemite nanoparticles releases Fe^{3+} only [24]. These structural and ionic release differences explain previously reported higher toxic profiles of magnetite nanoparticles compared to maghemite nanoparticles [25]. Thus, the accumulated evidence illustrates the therapeutic potential of magnetite nanoparticles in melanoma treatment; however, to the best of found knowledge, bare magnetite nanoparticles as an anti-melanoma agent has not been reported previously. In this context, in the current study, dose- and time-dependent selective toxicity of the bare magnetite nanoparticles on two different melanoma cell lines (A375 and G361 cells) has been investigated, using normal human umbilical vein/vascular endothelium cell line (HUVEC) as control.

2. MATERIALS AND METHODS

Melanoma cell lines (A375 and G361 cells), normal human umbilical vein/vascular endothelium cell line (HUVEC) and culture media components (Dulbecco's Modified Eagle's Medium (DMEM), McCoy's 5A Medium, Dimethylsulfoxide (DMSO), Fetal Bovine Serum (FBS), penicillin/streptomycin, Trypsin-EDTA Solution) were purchased from American Type Culture Collection (ATCC, Manassas, VA, USA). Iron (III) chloride hexahydrate (FeCl3.6H2O) pure granulated, 99%, iron (II) chloride tetrahydrate (FeCl2.4H2O) 99+%, ammonium hydroxide (5 M), HCl, Dichloro-dihydro-fluorescein diacetate (DCFH-DA), MTT (3- (4,5-dimethylthiazol- 2- yl)- 2,5- diphenyl - tetrazolium bromide) assay kit and Caspase 3 Assay Kit were purchased from Sigma Aldrich (Saint Louis, MO, USA). The Cell Death Detection ELISA Kit was purchased from Roche Diagnostic GmbH (Mannheim, Germany).

2.1. Synthesis of Magnetite (Fe_3O_4) Nanoparticles.

Synthesis of magnetite (Fe_3O_4) iron oxide nanoparticles (MION) was carried out as described in a previous study [5]. Briefly, 2 M $FeCl_2.4H_2O$ in 1 ml 2 M HCl (0.4 g $FeCl_2.4H_2O$ was dissolved in 1 ml 2 M HCl) and 1 M $FeCl_3.6H_2O$ in 4ml 2 M HCl (1.08 g $FeCl_3.6H_2O$ was dissolved in 4 ml 2 M HCl) were mixed and 50 ml of 1 M NH_3 solution were added dropwise over 5 min, while stirring on a magnetic stir plate. The formation of magnetite particles was indicated by the immediate turning of the suspension color to black. Using centrifugation (30000 rpm for 20 min), the particles were washed 3 times. Before subsequent centrifugation, the supernatant was discarded and the sediment was redispersed in 15 ml of nitrogen purged deionized water using sonication in a water-bath sonicator for 10 min. Following the third centrifugation, the particles were resuspended in water by sonication for 20 min and centrifuged at 1000 rpm for 20 min to remove any potentially large aggregates.

2.2. Characterization of Magnetite (Fe_3O_4) Nanoparticles.

The synthesized MION were characterized using FT-IR, XRD and particle size analyzer.

For FT-IR analyses, each spectrum was obtained by averaging 100 scans for each interferogram with a resolution of 2 cm^{-1}, using a PerkinElmer Spectrum 100 FT-IR spectrometer. Pellets were prepared by mixing lyophilized iron oxide nanoparticle samples with spectroscopic grade KBr powder. With three different pellets giving the same spectra, each sample was scanned under identical conditions. For further analyses, the average spectra belong to three replicates were used.

Using a Rigaku D-Max/B horizontal diffractometer with Bragg-Brentano parafocusing geometry (Rigaku, The Woodlands, TX, USA), the XRD analysis of the lyophilized samples of the nanoparticles was carried out. The equipment involves a copper target X-ray tube with Cu KR radiation. The parameters were 2θ steps of 0.02°, 6 s of counting time per step, and 2θ ranging from 20° to 80°. ~15 mg of the lyophilized sample was sprinkled onto a low background quartz XRD holder coated with a thin layer of silicone grease to retain the sample.

The hydrodynamic diameter size, particle size distribution and zeta potential of the nanoparticles were measured using a particle size analyzer (Malvern Mastersizer 2000 and Malvern Nano ZS90, Malvern Instruments, Royston, UK) by diluting the nanosuspensions homogeneously from 100 µl to 2 ml in 10 mM NaCl-added deionized water that was purged with nitrogen gas. The measurements were performed in triplicate and expressed as the mean ± SD.

2.3. Cell Culture and Maintenance.

A375 and HUVEC cells were cultured in Dulbecco's Modified Eagle's Medium (DMEM) supplemented with 10% fetal bovine serum, and 1% penicillin/streptomycin; G361 cells were cultured in McCoy's 5A Medium supplemented with 10% fetal bovine serum, and 1% penicillin/streptomycin (10,000 I.U./ml of penicillin, 10,000 µg/ml of streptomycin). The cells were grown in poly-L-lysine-coated flasks at 37ºC, 5% CO_2, 95% air in a humidified incubator and confirmed free of mycoplasma infection through regular testing. Sub-culturing was performed at approximately 48 h intervals, and cell growth was monitored with an inverted microscope; to ensure the stability of cell line, cells were used for experiments within eight passages.

2.4. Intracellular ROS Level.

As previously described [26], oxidative stress was measured by the Dichloro-dihydro-fluorescein diacetate (DCFH-DA) assay. 2 x 10^4 cells were seeded in 96-well plates and incubated with DCFH-DA probe for 40 min. Cells were exposed to the synthesized MION (50-400 µg/ml), (the control group received medium only) and incubated at 37 °C for 24 h; then, the fluorescence of each sample was read at 485 nm (excitation) and 527 nm (emission) wavelengths using a microplate reader. The intracellular ROS levels were expressed as fold change relative to the control group. Three different experiments were performed in triplicate in three different weeks.

2.5. Cytotoxicity Assay.

A375, G361 and HUVEC cells were seeded in culture plates and divided into three groups: I) Blank group containing medium without cells; II) Control group containing medium with cells that are not treated with MION; III) Test group containing medium with cells that are treated with different concentrations of the synthesized MION (50-400 µg/ml).

Using the MTT assay, cytotoxicity of the magnetite nanoparticles was evaluated. Cells in the logarithmic phase of growth were seeded in 96-well plates at a density of 1 × 10^4 cells/well; 24 h after seeding, the cells were exposed to the MION (50-400 µg/ml) for 24 h or 72 h (the control group received medium only) at 37 ºC and 5% CO_2/95% air in a humidified incubator, followed by incubated with 50 µL of MTT (5 mg/ml) for another 4 h. Using centrifugation (1250 rpm at 4 ºC for 5 minutes), the supernatant was removed; then, absorbance at 550 nm wavelength was measured using an ELISA reader following the addition of DMSO (100 µl). Three different experiments were performed in triplicate in three different weeks.

2.6. Live/Dead Assay.

To visualize the viability of the cells exposed to the synthesized MION, live/dead assay was performed at the end of treatments using a Live/Dead Viability/Cytotoxicity Kit (L- 3224 Invitrogen, Grand Island, NY) with assay reagent (4 µM EthD-1 and 2 µM Calcein in PBS).

2.7. Apoptosis.

As previously described [27], the Cell Death Detection ELISA Kit (Roche Diagnostic GmbH, Germany) was used to detect apoptosis in cells exposed to the synthesized MION. Briefly, cells in the logarithmic phase of growth were seeded in 96-well plates at

a density of 1×10^4 cells/well; after 24h of treatment with the MION (50-400 μg/ml) (the control group received medium only) the supernatants and lysate of cells were extracted and incubated in the microtiter plate modules coated with streptavidin. Subsequently, a mixture of anti-histone-biotin and peroxidase-conjugated anti-DNA antibody was used to detect immobilized histone/DNA fragments. Finally, using an ELISA reader, absorbance values at 405 nm were measured. The apoptosis was expressed as a fold change of absorbance value over that of the control group. Three different experiments were performed in triplicate in three different weeks.

2.8. Caspase-3 Assay.

As previously described [28], the activity of CPP32/caspase-3 was determined in cell extracts, using a Colorimetric Caspase 3 Assay Kit (Sigma Aldrich, Saint Louis, MO, USA). Briefly, the cells were exposed to the synthesized MION (50-400 μg/ml) (the control group received medium only) for 24 h, collected and lysed with cell lysis buffer. The cleavage of colorimetric peptide substrate was monitored by pNA (p-nitroanilide) liberation at 405 nm using a microtiter plate reader following incubation of the cell lysate with reaction buffer containing 5 μL of peptide substrate (DEVD-pNA) for 2 h at 37 °C. The activity was expressed as a fold change of absorbance value over that of the control group. Three different experiments were performed in triplicate in three different weeks.

2.9. Statistical Analyses.

To determine whether there were any statistically significant differences between the means of the groups, one-way analysis of variance (ANOVA) with Tukey's HSD (honestly significant difference) test was used. Data were expressed as the mean ± standard deviation (SD) from three independent experiments performed in replicates. For all the statistical analyses, $p<0.05$ was used as the threshold for significance.

3. RESULTS

FT-IR and XRD analyses were used to characterize the purity of magnetite (Fe_3O_4) nanoparticles. The characteristic bands of the magnetite nanoparticles are represented by the average FT-IR spectrum (Figure 1A) of the synthesized nanoparticles. Two absorption bands at around 580 cm^{-1} and 440 cm^{-1} represent Fe–O stretching bond vibrations in tetrahedral and octahedral sites, respectively; these bands represent the formation of the spinel-type structure of pure Fe_3O_4. The absorption bands at around 3400 cm^{-1} and 1630 cm^{-1} are indicative of stretching vibration and bending vibration, respectively; these bands represent hydroxyl groups on the surface of magnetite nanoparticles due to aqueous media synthesis [29-33]. The X-ray powder diffraction pattern (Figure 1B) for the synthesized iron oxide nanoparticles agrees with the pattern of magnetite particles listed in the American Society for Testing and Materials (ASTM) XRD standard card [34, 35]. Peak positions at 30, 35.5, 43, 53, 57 and 63, marked by their indices [(220), (311), (400), (422), (511), and (440)] are consistent with the standard data for magnetite XRD spectra. Thus, the XRD analyses strongly support the assignment of the synthesized iron oxide nanoparticle cluster as magnetite (Fe_3O_4).

Using a particle size analyzer, the apparent hydrodynamic radii and their distributions in the magnetite nanoparticle suspensions were measured. As illustrated in Figure 1C, the mean sizes of the synthesized MION were determined as 45.36 ± 0.33 nm. Mean zeta potential and polydispersity index (PDI) values of the MION were measured as -28.3 ± 0.82 mV and 0.20 ± 0.02, respectively.

Therapeutic nanoparticles between 10 and 100 nm are more effective relative to larger particles since their diffusion into the extracellular space is not restricted and they more easily reach cancer cells [36]. Thus, the synthesized MION (45.36 ± 0.33 nm) are in the effective size range for their use in biomedical applications. Synthesis of the MION involves a change in reaction media from acidic pH to basic pH due to the dissolving of $FeCl_3.6H_2O$ and $FeCl_2.4H_2O$ in HCl, followed by the addition of NH_3. Due to the increase in the H^+ ion concentration in acidic pH, nanoparticles have positive zeta potential; while due to the increase in OH^- ion concentration in basic pH, nanoparticles have negative zeta potential [37, 38]. The basic reaction media caused by the addition of NH_3 explains the measured negative zeta potential value for the synthesized MION. Positive or negative zeta potentials greater than 30 mV lead to monodispersity, while values less than 5 mV can cause agglomeration [39]. On the other hand, the polydispersity index (PDI) basically indicates the distribution of size populations; the PDI value ranges from 0.0, which represents an excellent uniform sample relative to particle size, to 1.0, which represents a highly polyydispersible sample with multiple particle size populations [40]. Thus, the mean zeta potential value (-28.3 ± 0.82 mV) far from zero and the near-zero PDI value (0.20 ± 0.02) of the synthesized MION indicate that the nanoparticles disperse well in the media due to the large electrostatic repulsive force among the particles, and the particles have high aqueous stability in the conditions in which they are to be used [41, 42]. These mechanisms have led to the observation that the synthesized MION have good dispersion stability in all experimental media throughout the study. All these highly advantageous properties make the synthesized MION quite attractive vehicles for biomedical applications.

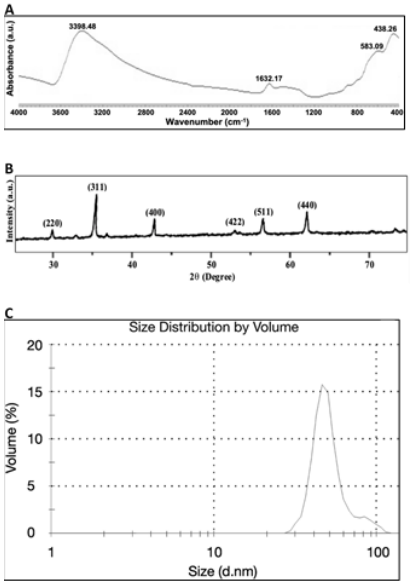

Figure 1. FT-IR spectrum, XRD powder pattern and particle size distribution of the synthesized MION. A: Average FT-IR spectrum of the replicates; B: XRD powder pattern; C: Hydrodynamic radius distributions.

3.1. The effect of the synthesized MION on intracellular ROS levels in normal (HUVEC) and melanoma (A375 and G361) cells.

ROS production capability of the synthesized MION in the normal (HUVEC) and melanoma (A375 and G361) cells were analyzed, and the results are presented in Figure 2. After 24 h incubation with different concentrations of the MION (50-400 μg/ml), highly significant ($p<0.01$) dose-dependent increases in ROS levels in normal and melanoma cells were observed, especially in the case of the MION in 200 and 400 μg/ml. On the other hand, each cell type has significantly ($p<0.01$) different responses to the MION in lower concentrations (50 and 100 μg/ml), compared to the other two cell types.

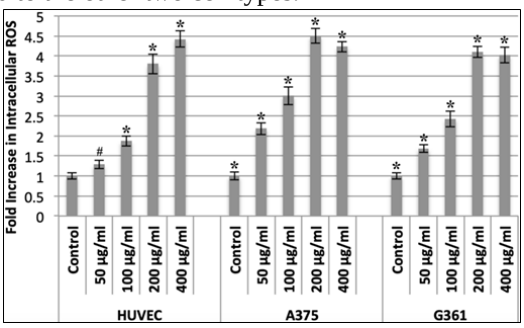

Figure 2. The effect of the synthesized MION on intracellular ROS levels in normal (HUVEC) and melanoma (A375 and G361) cells. Normal (HUVEC) and melanoma (A375 and G361) cells were treated with different concentrations of MION for 24 hours. Following treatment, the levels of ROS were determined as described in Materials and Methods. Significant difference with respect to control is denoted as $^{\#}p$ value <0.05 and $^{*}p$ value <0.01. 50 and 100 μg/ml of the MION caused significantly ($p<0.01$) higher fold increase in ROS between normal (HUVEC) and melanoma (A375 and G361) cells as well as between A375 and G361 cells.

Accumulating evidence in the literature strongly suggests that metal oxide nanoparticles including bare iron oxide nanoparticles used in the current study (Fe_3O_4) induce significant ROS production [7, 8, 23, 43]. Upon internalization by various intracellular uptake mechanisms including passive diffusion, receptor-mediated endocytosis, clathrin-mediated endocytosis, caveolin-mediated internalization and other clathrin and caveolin-independent endocytosis, magnetite (Fe_3O_4) iron oxide nanoparticles are degraded into the ferrous form of iron ions (Fe^{2+}) in the lysosomes (Equation 1). Crossing of these unbound free iron ions through the mitochondrial membrane is a major source of iron oxide nanoparticle-induced ROS production. Superoxide ($O_2^{\bullet -}$), a byproduct of oxidative phosphorylation, is produced by the mitochondrial electron transport chain from one-electron reduction of oxygen, and converted to hydrogen peroxide (H_2O_2) by superoxide dismutases [44, 45]. The unbound free iron ions released from iron oxide nanoparticles induce a wide range of ROS by serving as catalyst through the Fenton reaction (Equations 2 and 3, in which H_2O_2 is converted into highly reactive hydroxyl or superoxide radicals catalyzed by ferrous [Fe^{2+}]/ferric [Fe^{3+}] ions) and the Haber–Weiss reaction (Equation 5, which is the net reaction of Fenton reaction [Equation 2] and the reaction 4 in which superoxide [$O_2^{\bullet -}$] reduces the ferric ion [Fe^{3+}] released by the Fenton reaction) [7, 46].

$$Fe_3O_4 + 2H^+ \rightarrow Fe_2O_3 + Fe^{2+} + H_2O \quad (1)$$

$$Fe^{2+} + H_2O_2 \rightarrow Fe^{3+} + OH^- + OH^{\bullet} \quad (2)$$

$$Fe^{3+} + H_2O_2 \rightarrow Fe^{2+} + HO_2^{\bullet}/O_2^{\bullet -} + H^+ \quad (3)$$

$$Fe^{3+} + O_2^{\bullet -} \rightarrow Fe^{2+} + O_2 \quad (4)$$

$$O_2^{\bullet -} + H_2O_2 \rightarrow O_2 + OH^- + OH^{\bullet} \quad (5)$$

Ferric ion (Fe^{3+}) might also be reduced by a range of cellular reductants, such as glutathione, l-cysteine, NAD(P)H and $FADH_2$ (Equation 6) [47, 48]. Hydroxyl radical yielded by Fenton and Haber–Weiss reactions is by far the most ROS and is generally indicative of an overtly toxic event; $OH^{\bullet}$ reacts with biomolecules to form a series of additional free radicals (the thiyl radical [$RS^{\bullet}$] in Equation 7; a carbon-centred radical ($(R)_3C^{\bullet}$) in Equation 8; and the peroxyl radical ($(R)_3COO^{\bullet}$) in Equation 9) that can lead to oxidative stress, mitochondrial damage, lipid peroxidation, protein modification, DNA damage, cytotoxicity and genotoxicity [24, 47, 49, 50].

$$Fe^{3+} + \text{reduced antioxidant} \rightarrow Fe^{2+} + \text{oxidized antioxidant} \quad (6)$$

$$OH^{\bullet} + RSH \rightarrow H_2O + RS^{\bullet} \quad (7)$$

$$OH^{\bullet} + (R)_3CH \rightarrow H_2O + (R)_3C^{\bullet} \quad (8)$$

$$(R)_3C^{\bullet} + O_2 \rightarrow (R)_3COO^{\bullet} \quad (9)$$

Above-mentioned detailed mechanisms of ROS production induced by magnetite (Fe_3O_4) iron oxide nanoparticles offer an interesting therapeutic window for cancer, since accumulating evidence strongly suggests that cancer cells are more sensitive to ROS levels compared to healthy cells [23, 51, 52]. Therefore, upon treatment with four different concentrations (50, 100, 200 and 400 μg/ml) of the synthesized MION, ROS generation in the normal (HUVEC) and melanoma (A375 and G361) cells was investigated. After 24 h incubation, the MION caused highly significant ($p<0.01$) dose-dependent increase in ROS levels in normal and melanoma cells (Figure 2).

3.2. The effect of the synthesized MION on viability of normal (HUVEC) and melanoma (A375 and G361) cells.

In addition to their attractive characteristics, the fact that MION induces production of ROS suggests that they may have anti-cancer activity in melanoma cells. The cytotoxic effect of the synthesized MION (50-400 μg/ml) on the normal (HUVEC) and melanoma (A375 and G361) cells was analyzed using MTT assay, and the results are presented in Figure 3. After 24 h and 72 h incubation with different concentrations of the MION (50-400 μg/ml), highly significant ($p<0.01$) dose-dependent decreases in viability of the normal and melanoma cells were observed. On the other hand, according to the damage in viability of the cell types, the order from the least to the most serious is HUVEC<G361<A375, for all concentrations and incubation times. Statistical analyses illustrated that compared to normal cells (HUVEC), 24-h treatment with MION induced highly significant ($p<0.01$) damages in viability of A375 melanoma cells in the concentrations of 100, 200 and 400 μg/ml, while 24-h treatment with MION induced highly significant ($p<0.01$) damages in viability of G361 melanoma cells in the concentrations of 200 and 400 μg/ml; on the other hand, compared to normal cells (HUVEC), 72-h treatment with MION induced highly significant ($p<0.01$) damages in viability of A375 melanoma cells in all of the concentrations (50, 100, 200 and 400 μg/ml), while 72-h treatment

with MION induced highly significant ($p<0.01$) damages in viability of G361 melanoma cells in the concentrations of 200 and 400 µg/ml.

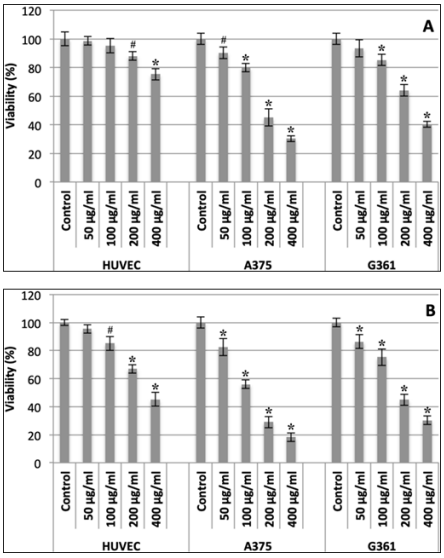

Figure 3. The effect of the synthesized MION on the viability of normal (HUVEC) and melanoma (A375 and G361) cells. Normal (HUVEC) and melanoma (A375 and G361) cells were treated with different concentrations of MION for 24 hours or 72 hours. Following treatment, cell viability was assessed by the MTT assay as described in Materials and Methods. A: 24 h treatment with MION; B: 72 h treatment with MION. Significant difference with respect to control is denoted as $^{\#}p$ value <0.05 and $^{*}p$ value <0.01. Statistical analyses between different cells: A: HUVEC vs. A375: $p<0.01$ for 100-400 µg/ml treatment; HUVEC vs. G361 and A375 vs. G361: $p<0.01$ for 200 and 400 µg/ml treatment; B: HUVEC vs. A375: $p<0.01$ for 50-400 µg/ml treatment; HUVEC vs. G361: $p<0.01$ for 200 and 400 µg/ml treatment; A375 vs. G361: $p<0.01$ for 100-400 µg/ml treatment.

Using MTT cell viability assay, the half-maximal (50%) inhibitory concentration (IC_{50}) values of the synthesized MION were determined for normal and melanoma cells and the results are presented in Table 1.

Table 1. IC_{50} (µg/ml) values of the synthesized MION for the viability of normal (HUVEC) and melanoma (A375 and G361) cells. Results were expressed as the mean of triplicates ± SD.

Cells	24h	72h
HUVEC	549.37 ± 20.48	270.69 ± 13.35
A375	152.02 ± 7.34	102.56 ± 6.64
G361	219.93 ± 15.76	151.41 ± 8.61

The representative live/dead images (Figure 4) belong to normal (HUVEC) and melanoma (A375 and G361) cells treated with the synthesized MION (200 µg/ml) support the mentioned viability results.

The results (Table 1, Figure 3 and 4) illustrated that the synthesized MION selectively decreased cell viability of melanoma cells in a dose- and time-dependent manner. Accumulating evidence strongly suggests that metal nanoparticles selectively target mitochondria [23]; consistently, MTT assay results revealed by the current study illustrate selectively mitochondria targeting of the synthesized MION. Since, the assay measures conversion of the tetrazolium compound to water insoluble formazan crystals by mainly mitochondrial dehydrogenases in living cells [24, 53].

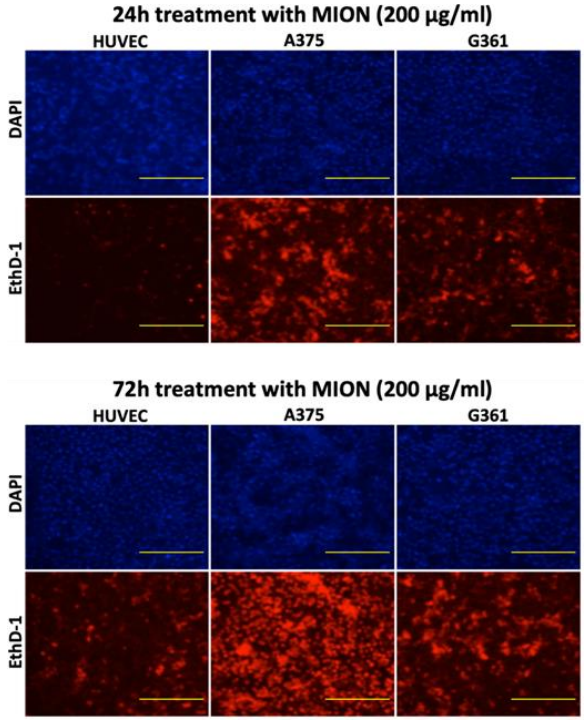

Figure 4. The representative live/dead images of normal (HUVEC) and melanoma (A375 and G361) cells. Following the treatment of HUVEC, A375 and G361 cells with the MION (200 µg/ml) for 24 h or for 72 h, live/dead assay was performed as described in Materials and Methods. Blue: DNA/nuclei of the cells; Red: Dead cells. Image scale bar: 400 µm.

Therefore, the measurement can be used as an indicator of mitochondrial and metabolic activity. Metal oxide nanoparticles induce mitochondrial toxicity that is primarily mediated by increased ROS production [7, 23]. Redox control might induce one of the following outcomes in cancer cells: At low levels, free radicals promote cell proliferation by activating signaling pathways; at moderate levels, free radicals promote stress responsive genes (e.g., HIF-1α) and cell survival; while at high levels, free radicals cause macromolecular and organelle damage, triggering senescence or apoptosis, and in surviving cells, activating antioxidant pathways [52, 54]. Thus, ROS levels are regulated by powerful antioxidant defense mechanisms in cancer cells, but they remain higher than those in normal cells [23, 51, 52, 55]. The differences in ROS levels between normal (HUVEC) and melanoma (A375 and G361) cells before the treatment with MION explains the differential outcome on the fold increase in ROS levels between normal and melanoma cells after the treatment with MION. Although treatment with 200 and 400 µg/ml MION resulted in a comparable fold increase in ROS levels in both normal and melanoma cells (Figure 2), more dramatic dose- and time-dependent effect on the viability of melanoma cells was observed (Table 1, Figure 3 and 4). In other words, the levels of ROS, which are initially low in healthy cells, reached far more harmful levels in cancer cells after the MION treatment. Thus, 24 h treatment of <549.37 ± 20.48 µg/ml MION (IC_{50} value of 24 h treatment for HUVEC cells) and 72 h treatment of <270.69 ± 13.35 µg/ml MION (IC_{50} value of 72 h treatment for HUVEC cells) are quite effective for selectively killing the melanoma cells.

The dose-dependent effect of the synthesized MION on apoptosis was analyzed, and the results are presented in Figure 5A. The role of caspase-3 activity in the apoptosis of cells was also investigated (Figure 5B).

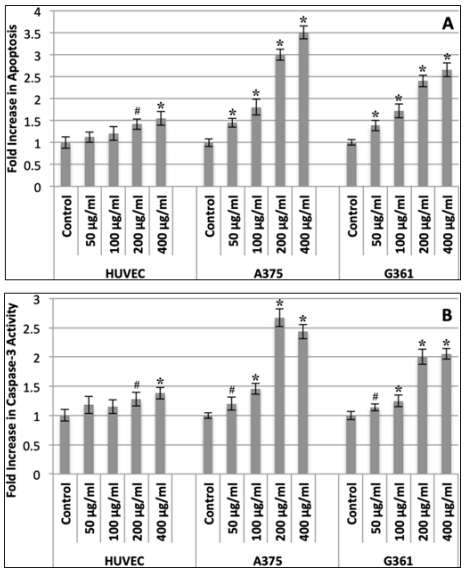

Figure 5. The effect of the synthesized MION on apoptosis and caspase-3 activity in normal (HUVEC) and melanoma (A375 and G361) cells. Normal (HUVEC) and melanoma (A375 and G361) cells were treated with different concentrations of MION for 24 hours. Apoptosis and caspase-3 activity were examined as described in the Materials and Methods. A: Apoptosis; B: Caspase-3 activity. Significant difference with respect to control is denoted as $^{\#}p$ value <0.05 and $^{*}p$ value <0.01. Statistical analyses between different cells: A: HUVEC vs. A375 and HUVEC vs. G361: $p<0.05$ for 50 and 100 µg/ml treatment, $p<0.01$ for 200 and 400 µg/ml treatment; A375 vs. G361: $p<0.01$ for 200 and 400 µg/ml treatment; B: HUVEC vs. A375: $p<0.05$ for 100 µg/ml treatment, $p<0.01$ for 200 and 400 µg/ml treatment; HUVEC vs. G361 and A375 vs. G361: $p<0.01$ for 200 and 400 µg/ml treatment.

3.3. The effect of the synthesized MION on Apoptosis/Caspase-3 Activity of normal (HUVEC) and melanoma (A375 and G361) cells.

Consistently with the viability results, the lowest apoptosis and caspase-3 activity rates were observed in HUVEC cells, while the highest apoptosis and caspase-3 activity rates were observed in A375 cells. Statistical analyses illustrated that compared to normal cells (HUVEC), 24-h treatment with MION induced significant ($p<0.05$) increases in apoptosis both in A375 and G361 melanoma cells in the concentrations of 50 and 100 µg/ml, and induced highly significant ($p<0.01$) increases in apoptosis both in A375 and G361 melanoma cells in the concentrations of 200 and 400 µg/ml; on the other hand, compared to normal cells (HUVEC), 24-h treatment with MION (100 µg/ml) induced significant ($p<0.05$) increases and with MION (200 and 400 µg/ml) induced highly significant ($p<0.01$) increases in caspase-3 activity in A375 melanoma cells, while 24-h treatment with MION (200 and 400 µg/ml) induced highly significant ($p<0.01$) increases in caspase-3 activity in G361 melanoma cells.

All concentrations of MION caused highly significant ($p<0.01$) increases in apoptosis rate in melanoma cells, while only 200 µg/ml ($p<0.05$) and 400 µg/ml ($p<0.01$) of MION caused significant increases in apoptosis rate in normal cells (Figure 5A). Caspase-3 activity is a crucial event leading to apoptosis; among many members of the caspase family, caspase-3 is the final executor of apoptotic DNA damage and its activation is widely used as a marker of apoptosis [56, 57]. Therefore, the activity of caspase-3 in normal and melanoma cells was measured to investigate whether caspase signal cascade is involved in MION-induced apoptosis; caspase-3 activity (Figure 5B) was found to be highly compatible with apoptosis (Figure 5A). There are two main apoptotic pathways (the extrinsic (death receptor) pathway and the intrinsic (mitochondrial) pathway) that can initiate the activation of caspases in response to anticancer compounds [58, 59]. ROS production causes an increased ratio of Bax to Bcl-2 gene expression, then the mitochondrial pathway is initiated by the release of apoptogenic factors such as cytochrome c; the release of cytochrome c into the cytosol triggers caspase-3 activation, which results in apoptosis [59-61]. These cellular pathways are consistent with the anti-melanoma activity of the synthesized MION; since the MION activity has been characterized by selectively targeting mitochondria in cancer cells that induces ROS-mediated caspase-3 activation and apoptosis. In addition, DNA damages caused by the free Fe^{2+} ions released from the MION as well as the ROS produced in mitochondria can contribute to the toxicity by the mitochondrial pathway through apoptosis, genotoxicity, mutagenicity, and cell death [8, 61]; and further researches need to be conducted to clarify this issue.

On the other hand, viability, apoptosis and caspase-3 activity assays illustrate that G361 melanoma cells are more resistant to the treatment with MION compared to A375 melanoma cells. Based on detailed microarray analyses, the antioxidant, pro-survival gene, ATOX1, is up-regulated, and the pro-apoptotic gene, CASP4, is down-regulated in G361 cells, but they remain uninduced in A375 cells. In addition, based on detailed qRT-PCR results, compared to A375 cells, there is significant up-regulation of 3 anti apoptotic genes and the antioxidant gene for glutathione reductase in G361 cells [62, 63]. The combination of these factors explains why G361 cells are more resistant than A375 cells to the treatment with MION.

It should be pointed out that the synthesized MION have a handicap -high IC_{50} values for melanoma cells-; although the nanoparticles have much lower IC_{50} values for melanoma (A375 and G361) cells compared to normal (HUVEC) cells, the IC_{50} values for melanoma cells (219.93 ± 15.76 and 152.02 ± 7.34 µg/ml for 24h-treated G361 and A375 cells, respectively; 151.41 ± 8.61 and 102.56 ± 6.64 µg/ml for 72h-treated G361 and A375 cells, respectively) may raise concerns that nanoparticles can cause side effects when they are used for melanoma treatment. Since previous studies [7, 8, 64-66] have reported low toxicity or cytotoxicity in normal cells caused by a range of iron oxide nanoparticles with varying physico-chemical characteristics at doses of 100 µg/ml or higher. On the other hand, due to their selective toxicity on melanoma cells, for further studies, the MION can be considered as a potent agent in combination therapies for melanoma treatment (e.g., sensitization of drug-resistant melanoma cells) allowing usage of lower amounts of the MION; for instance, the recent study from our laboratory has reported promising results on the sensitization of cisplatin-resistant ovarian cancer cells to cisplatin by magnetite iron oxide nanoparticles in ≤100 µg/ml [67].

4. CONCLUSIONS

In conclusion, the current study illustrated that: I- Based on hydrodynamic size, zeta potential and polydispersity index values, the synthesized magnetite nanoparticles are attractive vehicles for biomedical applications; II- ROS production capability of the synthesized magnetite nanoparticles induced a hypothesis that the nanoparticles may have potential selective anti-cancer activity; III-

As evidenced by the experimental results of the MTT assay using normal (HUVEC) and melanoma (A375 and G361) cells, the synthesized magnetite nanoparticles (45.36 ± 0.33 nm) in the concentration range (50-400 µg/ml) have selectively decreased cell viability of the melanoma cells in a dose- and time-dependent manner; IV- As evidenced by the experimental results of the apoptosis and caspase-3 activity assays using normal (HUVEC) and melanoma (A375 and G361) cells, the synthesized magnetite nanoparticles (45.36 ± 0.33 nm) in the concentration range (50-400 µg/ml) have selectively increased apoptosis rate of the melanoma cells in a dose- and time-dependent manner by activating caspase-3; V- Viability, apoptosis and caspase-3 activity assays have illustrated that G361 melanoma cells are more resistant to the treatment with the synthesized magnetite nanoparticles (45.36 ± 0.33 nm) compared to A375 melanoma cells.

Thus, the results revealed by the current study suggest that the synthesized magnetite nanoparticles can act as a potent agent on melanoma treatment by inducing ROS mediated caspase-3 activation and apoptosis. On the other hand, although the nanoparticles have a handicap -high IC_{50} values for melanoma cells- that may raise safety concerns, due to their selective toxicity on melanoma cells they can also be considered as a potent agent in combination therapies for melanoma treatment (e.g., sensitization of drug-resistant melanoma cells) allowing usage of lower amounts of the nanoparticles. In this context, further studies on the sensitization of drug-resistant melanoma cells using iron oxide nanoparticles are ongoing in our group.

Since variations in the concentration and physicochemical properties of nanoparticles including magnetite nanoparticles such as size, shape and surface properties can change their behavior in the biological environment, further investigations on the anti-melanoma profiles of different sized and surface functionalized magnetite (Fe_3O_4) iron oxide nanoparticles continue in our laboratory. In addition, upon internalization by various intracellular uptake mechanisms, the degradation of iron oxide nanoparticles into iron ions is a crucial step affecting the bioactivity of these nanoparticles; in this context, further studies on the internalization, metabolization and DNA damaging potential of the iron oxide nanoparticles in cancer cells as well as the release profiles of iron ions from iron oxide nanoparticles and their effects on cancer cells are also ongoing in our group.

5. REFERENCES

1. Bray, F.; Ferlay, J.; Soerjomataram, I.; Siegel, R.L.; Torre, L.A.; Jemal, A. Global cancer statistics 2018: GLOBOCAN estimates of incidence and mortality worldwide for 36 cancers in 185 countries. *CA Cancer J Clin* **2018**, *68*, 394-424, https://doi.org/10.3322/caac.21492.
2. Mishra, H.; Mishra, P.K.; Ekielski, A.; Jaggi, M.; Iqbal, Z.; Talegaonkar, S. Melanoma treatment: from conventional to nanotechnology. *J Cancer Res Clin Oncol* **2018**, *144*, 2283-2302, https://doi.org/10.1007/s00432-018-2726-1.
3. El-Kenawy, A.E.M.; Constantin, C.; Hassan, S.M.A.; Mostafa, A.M.; Neves, A.F.; de Araújo, T.G.; Neagu, M. Nanomedicine in melanoma: Current trends and future perspectives. In: *Cutaneous Melanoma: Etiology and Therapy*. Ward, W.H.; Farma, J.M. Eds.; Codon Publications: Brisbane, AU, 2017; pp. 143-159.
4. Pautu, V.; Leonetti, D.; Lepeltier, E.; Clere, N.; Passirani, C. Nanomedicine as a potent strategy in melanoma tumor microenvironment. *Pharmacol Res* **2017**, *126*, 31-53, https://doi.org/10.1016/j.phrs.2017.02.014.
5. Gokduman, K.; Demir, A.S. Camptothecin anticancer drug loaded iron oxide micro and nanoparticles: Tuning targeted and sustained release of the drug in bioactive form. *Curr Nanosci* **2013**, *9*, 704-710, https://doi.org/10.2174/15734137113099990076.
6. Gokduman, K. Strategies targeting DNA topoisomerase I in cancer chemotherapy: Camptothecins, nanocarriers for camptothecins, organic non-camptothecin compounds and metal complexes. *Curr Drug Targets* **2016**, *17*, 1928-1939, https://doi.org/10.2174/1389450117666160502151707.
7. Gokduman, K.; Bestepe, F.; Li, L.; Yarmush, M.L.; Usta, O.B. Dose-, treatment- and time-dependent toxicity of superparamagnetic iron oxide nanoparticles on primary rat hepatocytes. *Nanomedicine* **2018**, *13*, 1267-1284, https://doi.org/10.2217/nnm-2017-0387.
8. Singh, N.; Jenkins, G.J.S.; Asadi, R.; Doak, S.H. Potential toxicity of superparamagnetic iron oxide nanoparticles (SPION). *Nano Rev* **2010**, *1*, 5358, https://doi.org/10.3402/nano.v1i0.5358.
9. Dey, S.; Maiti, T.K. Superparamagnetic nanoparticles and RNAi-mediated gene silencing: evolving class of cancer diagnostics and therapeutics. *J Nanomater* **2012**, *2012*, https://doi.org/10.1155/2012/129107.
10. Estelrich, J.; Escribano, E.; Queralt, J.; Busquets, M.A. Iron oxide nanoparticles for magnetically guided and magnetically responsive drug delivery. *Int J Mol Sci* **2015**, *16*, 8070-8101, https://doi.org/10.3390/ijms16048070.
11. Kandasamy, G.; Maity, D. Recent advances in superparamagnetic iron oxide nanoparticles (SPIONs) for in vitro and in vivo cancer nanotheranostics. *Int J Pharm* **2015**, *496*, 191-218, https://doi.org/10.1016/j.ijpharm.2015.10.058.
12. Ortgies, D.H.; de la Cueva, L.; Del Rosal, B.; Sanz-Rodríguez, F.; Fernández, N.; Iglesias-de la Cruz, M.C.; Salas, G.; Cabrera, D.; Teran, F.J.; Jaque, D.; Martín Rodríguez, E. In vivo deep tissue fluorescence and magnetic imaging employing hybrid nanostructures. *ACS Appl Mater Interfaces* **2016**, *8*, 1406-1414, https://doi.org/10.1021/acsami.5b10617.
13. Wu, S.C.; Chen, Y.J.; Wang, H.C.; Chou, M.Y.; Chang, T.Y.; Yuan, S.S.; Chen, C.Y.; Hou, M.F.; Hsu, J.T.A.; Wang, Y.M. Bispecific antibody conjugated manganese-based magnetic engineered iron oxide for imaging of HER2/neu- and EGFR-expressing tumors. *Theranostics* **2016**, *6*, 118-130, https://doi.org/10.7150/thno.13069.
14. Mu, Q.; Kievit, F.M.; Kant, R.J.; Lin, G.; Jeon, M.; Zhang, M. Anti-HER2/neu peptide-conjugated iron oxide nanoparticles for targeted delivery of paclitaxel to breast cancer cells. *Nanoscale* **2015**, *7*, 18010-18014, https://doi.org/10.1039/c5nr04867b.
15. Wang, K.; Kievit, F.M.; Sham, J.G.; Jeon, M.; Stephen, Z.R.; Bakthavatsalam, A.; Park, J.O.; Zhang, M. Iron-oxide-based nanovector for tumor targeted siRNA delivery in an orthotopic hepatocellular carcinoma xenograft mouse model. *Small* **2016**, *12*, 477-487, https://doi.org/10.1002/smll.201501985.
16. Xiao, S.; Castro, R.; Rodrigues, J.; Shi, X.; Tomas, H. PAMAM dendrimer/pDNA functionalized-magnetic iron oxide nanoparticles for gene delivery. *J Biomed Nanotechnol* **2015**, *11*, 1370-1384, https://doi.org/10.1166/jbn.2015.2101.
17. Bradshaw, M.; Clemons, T.D.; Ho, D.; Gutiérrez, L.; Lázaro, F.J.; House, M.J.; St Pierre, T.G.; Fear, M.W.; Wood, F.M.; Iyer, K.S. Manipulating directional cell motility using intracellular superparamagnetic nanoparticles. *Nanoscale* **2015**, *7*, 4884-4889, https://doi.org/10.1039/c4nr06594h.

18. Jia, Y.; Fan, M.; Chen, H.; Miao, Y.; Xing, L.; Jiang, B.; Cheng, Q.; Liu, D.; Bao, W.; Qian, B.; Wang, J.; Xing, X.; Tan, H.; Ling, Z.; Chen, Y. Magnetic hyaluronic acid nanospheres via aqueous Diels–Alder chemistry to deliver dexamethasone for adipose tissue engineering. *J Colloid Interface Sci* **2015**, *458*, 293-299, https://doi.org/10.1016/j.jcis.2015.07.062.
19. Kossatz, S.; Grandke, J.; Couleaud, P.; Latorre, A.; Aires, A.; Crosbie-Staunton, K.; Ludwig, R.; Dähring, H.; Ettelt, V.; Lazaro-Carrillo, A.; Calero, M.; Sader, M.; Courty, J.; Volkov, Y.; Prina-Mello, A.; Villanueva, A.; Somoza, Á.; Cortajarena, A.L.; Miranda, R.; Hilger, I. Efficient treatment of breast cancer xenografts with multifunctionalized iron oxide nanoparticles combining magnetic hyperthermia and anti-cancer drug delivery. *Breast Cancer Res* **2015**, *17*, 66, https://doi.org/10.1186/s13058-015-0576-1.
20. Quinto, C.A.; Mohindra, P.; Tong, S.; Bao, G. Multifunctional superparamagnetic iron oxide nanoparticles for combined chemotherapy and hyperthermia cancer treatment. *Nanoscale* **2015**, *7*, 12728-12736, https://doi.org/10.1039/c5nr02718g.
21. Pang, P.; Wu, C.; Gong, F.; Zhu, K.; Meng, X.; Cheng, D.; Hu, X.; Shan, H.; Shuai, X. Nanovector for gene transfection and MR imaging of mesenchymal stem cells. *J Biomed Nanotechnol* **2015**, *11*, 644–656, https://doi.org/10.1166/jbn.2015.1967.
22. Wu, C.; Li, J.; Pang, P.; Liu, J.; Zhu, K.; Li, D.; Cheng, D.; Chen, J.; Shuai, X.; Shan, H. Polymeric vector-mediated gene transfection of MSCs for dual bioluminescent and MRI tracking in vivo. *Biomaterials* **2014**, *35*, 8249-8260, https://doi.org/10.1016/j.biomaterials.2014.06.014.
23. Naserzadeh, P.; Ansari Esfeh, F.; Kaviani, M.; Ashtari, K.; Kheirbakhsh, R.; Salimi, A.; Pourahmad, J. Single-walled carbon nanotube, multi-walled carbon nanotube and Fe2O3 nanoparticles induced mitochondria mediated apoptosis in melanoma cells. *Cutan Ocul Toxicol* **2018**, *37*, 157-166, https://doi.org/10.1080/15569527.2017.1363227.
24. Patil, U.S.; Adireddy, S.; Jaiswal, A.; Mandava, S.; Lee, B.R.; Chrisey, D.B. In vitro/in vivo toxicity evaluation and quantification of iron oxide nanoparticles. *Int J Mol Sci* **2015**, *16*, 24417-24450, https://doi.org/10.3390/ijms161024417.
25. Park, E.J.; Umh, H.N.; Choi, D.H.; Cho, M.H.; Choi, W.; Kim, S.W.; Kim, Y.; Kim, J.H. Magnetite- and maghemite-induced different toxicity in murine alveolar macrophage cells. *Arch Toxicol* **2014**, *88*, 1607-1618, https://doi.org/10.1007/s00204-014-1210-1.
26. Aranda, A.; Sequedo, L.; Tolosa, L.; Quintas, G.; Burello, E.; Castell, J.V.; Gombau, L. Dichloro-dihydro-fluorescein diacetate (DCFH-DA) assay: a quantitative method for oxidative stress assessment of nanoparticle-treated cells. *Toxicol In Vitro* **2013**, *27*, 954-963, https://doi.org/10.1016/j.tiv.2013.01.016.
27. Orangi, M.; Pasdaran, A.; Shanehbandi, D.; Kazemi, T.; Yousefi, B.; Hosseini, B.A.; Baradaran, B. Cytotoxic and apoptotic activities of methanolic subfractions of scrophularia oxysepala against human breast cancer cell line. *Evid Based Complement Alternat Med* **2016**, *2016*, 8540640, https://doi.org/10.1155/2016/8540640.
28. Ucar, M.; Deger, O.; Gerigelmez, A.Y.; Cengiz, S.; Barlak, Y.; Ovalı, E. Effect of Turkish pollen and propolis extracts on caspase-3 activity in myeloid cancer cell lines. *Trop J Pharm Res* **2016**, *15*, 2445-2449, https://doi.org/10.4314/tjpr.v15i11.20.
29. Mohammadi, A.; Barikani, M. Synthesis and characterization of superparamagnetic Fe3O4 nanoparticles coated with thiodiglycol. *Mater Charact* **2014**, *90*, 88-93, https://doi.org/10.1016/j.matchar.2014.01.021.
30. Arokiyaraj, S.; Saravanan, M.; Udaya Prakash, N.K.; Valan Arasu, M.; Vijayakumar, B.; Vincent, S. Enhanced antibacterial activity of iron oxide magnetic nanoparticles treated with Argemone mexicana L. leaf extract: An in vitro study. *Mater Res Bull* **2013**, *48*, 3323-3327, https://doi.org/10.1016/j.materresbull.2013.05.059.
31. Togashi, T.; Naka, T.; Asahina, S.; Sato, K.; Takamid, S.; Adschiri, T. Surfactant-assisted one-pot synthesis of superparamagnetic magnetite nanoparticle clusters with tunable cluster size and magnetic field sensitivity. *Dalton Trans* **2011**, *40*, 1073-1078, https://doi.org/10.1039/C0DT01280G.
32. Cheng, F.Y.; Su, C.H.; Yang, Y.S.; Yeh, C.S.; Tsai, C.Y.; Wu, C.L.; Wu, M.T.; Shieh, D.B. Characterization of aqueous dispersions of Fe3O4 nanoparticles and their biomedical applications. *Biomaterials* **2005**, *26*, 729-738, https://doi.org/10.1016/j.biomaterials.2004.03.016.
33. Saranya, T.; Parasuraman, K.; Anbarasu, M.; Balamurugan, K. XRD, FT-IR and SEM study of magnetite (Fe3O4) nanoparticles prepared by hydrothermal method. *Nano Vision* **2015**, *5*, 149-154.
34. Si, S.; Kotal, A.; Mandal, T.K.; Giri, S.; Nakamura, H.; Kohara, T. Size-controlled synthesis of magnetite nanoparticles in the presence of polyelectrolytes. *Chem Mater* **2004**, *16*, 3489-3496, https://doi.org/10.1021/cm049205n.
35. Gou, M.L.; Qian, Z.Y.; Wang, H.; Tang, Y.B.; Huang, M.J.; Kan, B.; Wen, Y.J.; Dai, M.; Li, X.Y.; Gong, C.Y.; Tu, M.J. Preparation and characterization of magnetic poly(epsilon-caprolactone)-poly(ethylene glycol)-poly(epsilon-caprolactone) microspheres. *J Mater Sci Mater Med* **2008**, *19*, 1033-1041, https://doi.org/10.1007/s10856-007-3230-3.
36. Chen, Z.G. Small-molecule delivery by nanoparticles for anticancer therapy. *Trends Mol Med* **2010**, *16*, 594-602, https://doi.org/10.1016/j.molmed.2010.08.001.
37. Illés, E.; Szekeres, M.; Tóth, I.Y.; Farkas, K.; Földesi, I.; Szabó, Á.; Iván, B.; Tombácz, E. PEGylation of superparamagnetic iron oxide nanoparticles with self-organizing polyacrylate-PEG brushes for contrast enhancement in MRI diagnosis. *Nanomaterials* **2018**, *8*, 776, https://doi.org/10.3390/nano8100776.
38. Patil, S.; Sandberg, A.; Heckert, E.; Self, W.; Seal, S. Protein adsorption and cellular uptake of cerium oxide nanoparticles as a function of zeta potential. *Biomaterials* **2007**, *28*, 4600-4607, https://doi.org/10.1016/j.biomaterials.2007.07.029.
39. Gumustas, M.; Sengel-Turk, C.T.; Gumustas, A.; Ozkan, S.A.; Uslu, B. Effect of Polymer-Based Nanoparticles on the Assay of Antimicrobial Drug Delivery Systems. In: *Multifunctional systems for combined delivery, biosensing and diagnostics*. 1st ed.; Grumezescu, A.M. Ed.; Elsevier Inc., Netherlands, 2017; pp. 67-108, https://doi.org/10.1016/B978-0-323-52725-5.00005-8.
40. Danaei, M.; Dehghankhold, M.; Ataei, S.; Hasanzadeh Davarani, F.; Javanmard, R.; Dokhani, A.; Khorasani, S.; Mozafari, M.R. Impact of particle size and polydispersity index on the clinical applications of lipidic nanocarrier systems. *Pharmaceutics* **2018**, *10*, 57, https://doi.org/10.3390/pharmaceutics10020057.
41. Goncalves, L.C.; Seabra, A.B.; Pelegrino, M.T.; Araujo, D.R.; Bernardesc, J.S.; Haddad, P.S. Superparamagnetic iron oxide nanoparticles dispersed in Pluronic F127 hydrogel: potential uses in topical applications. *RSC Adv* **2017**, *7*, 14496-14503, https://doi.org/10.1039/C6RA28633J.
42. Paik, S.Y.; Kim, J.S.; Shin, S.J.; Ko, S. Characterization, quantification, and determination of the toxicity of iron oxide nanoparticles to the bone marrow cells. *Int J Mol Sci* **2015**, *16*, 22243-22257, https://doi.org/10.3390/ijms160922243.
43. Natarajan, V.; Wilson, C.L.; Hayward, S.L.; Kidambi, S. Titanium dioxide nanoparticles trigger loss of function and perturbation of mitochondrial dynamics in primary hepatocytes.

PLoS ONE **2015**, *10*, e0134541, https://doi.org/10.1371/journal.pone.0134541.
44. Diebold, L.; Chandel, N.S. Mitochondrial ROS regulation of proliferating cells. *Free Radic Biol Med* **2016**, *100*, 86-93, https://doi.org/10.1016/j.freeradbiomed.2016.04.198.
45. Murphy, M.P. How mitochondria produce reactive oxygen species. *Biochem J* **2009**, *417*, 1-13, https://doi.org/10.1042/BJ20081386.
46. Shukla, S.; Jadaun, A.; Arora, V.; Sinha, R.K.; Biyani, N.; Jain, V.K. In vitro toxicity assessment of chitosan oligosaccharide coated iron oxide nanoparticles. *Toxicol Rep* **2015**, *2*, 27-39, https://doi.org/10.1016/j.toxrep.2014.11.002.
47. Lemire, J.A.; Harrison, J.J.; Turner, R.J. Antimicrobial activity of metals: mechanisms, molecular targets and applications. *Nat Rev Microbiol* **2013**, *11*, 371-384, https://doi.org/10.1038/nrmicro3028.
48. Imlay, J.A. Pathways of oxidative damage. *Annu Rev Microbiol* **2003**, *57*, 395-418, https://doi.org/10.1146/annurev.micro.57.030502.090938.
49. Kehrer, J.P. The Haber–Weiss reaction and mechanisms of toxicity. *Toxicology* **2000**, *149*, 43-50, https://doi.org/10.1016/s0300-483x(00)00231-6.
50. Fu, P.P.; Xia, Q.; Hwang, H.M.; Ray, P.C.; Yu, H. Mechanisms of nanotoxicity: generation of reactive oxygen species. *J Food Drug Anal* **2014**, *22*, 64-75, https://doi.org/10.1016/j.jfda.2014.01.005.
51. Liu, J.; Wang, Z.J. Increased oxidative stress as a selective anticancer therapy. *Oxid Med Cell Longev* **2015**, *2015*, 294303, https://doi.org/10.1155/2015/294303.
52. Trachootham, D.; Alexandre, J.; Huang, P. Targeting cancer cells by ROS-mediated mechanisms: a radical therapeutic approach? *Nat Rev Drug Discov* **2009**, *8*, 579-591, https://doi.org/10.1038/nrd2803.
53. van Tonder, A.; Joubert, A.M.; Cromarty, A.D. Limitations of the 3-(4,5-dimethylthiazol-2-yl)-2,5-diphenyl-2H-tetrazolium bromide (MTT) assay when compared to three commonly used cell enumeration assays. *BMC Res Notes* **2015**, *8*, 47, https://doi.org/10.1186/s13104-015-1000-8.
54. Feitelson, M.A.; Arzumanyan, A.; Kulathinal, R.J.; Blain, S.W.; Holcombe, R.F.; Mahajna, J.; Marino, M.; Martinez-Chantar, M.L.; Nawroth, R.; Sanchez-Garcia, I.; Sharma, D.; Saxena, N.K.; Singh, N.; Vlachostergios, P.J.; Guo, S.; Honoki, K.; Fujii, H.; Georgakilas, A.G.; Bilsland, A.; Amedei, A.; Niccolai, E.; Amin, A.; Ashraf, S.S.; Boosani, C.S.; Guha, G.; Ciriolo, M.R.; Aquilano, K.; Chen, S.; Mohammed, S.I.; Azmi, A.S.; Bhakta, D.; Halicka, D.; Keith, W.N.; Nowsheen, S. Sustained proliferation in cancer: Mechanisms and novel therapeutic targets. *Semin Cancer Biol* **2015**, *35*, S25-S54, https://doi.org/10.1016/j.semcancer.2015.02.006.
55. Sullivan, L.B.; Chandel, N.S. Mitochondrial reactive oxygen species and cancer. *Cancer Metab* **2014**, *2*, 17, https://doi.org/10.1186/2049-3002-2-17.
56. Cohen, G.M. Caspases: The executioners of apoptosis. *Biochem J* **1997**, *326*, 1-16, https://doi.org/10.1042/bj3260001.
57. Janicke, R.U.; Sprengart, M.L.; Wati, M.R.; Porter, A.G. Caspase-3 is required for DNA fragmentation and morphological changes associated with apoptosis. *J Biol Chem* **1998**, *273*, 9357-9360, https://doi.org/10.1074/jbc.273.16.9357.
58. Tomitaka, A.; Yamada, T.; Takemura, Y. Magnetic nanoparticle hyperthermia using pluronic-coated Fe3O4 nanoparticles: An in vitro study. *J Nanomater* **2012**, *2012*, 480626, https://doi.org/10.1155/2012/480626.
59. Fulda, S.; Debatin, K.M. Extrinsic versus intrinsic apoptosis pathways in anticancer chemotherapy. *Oncogene* **2006**, *25*, 4798-4811, https://doi.org/10.1038/sj.onc.1209608.
60. Maity, P.; Bepari, M.; Pradhan, A.; Baral, R.; Roy, S.; Maiti Choudhury, S. Synthesis and characterization of biogenic metal nanoparticles and its cytotoxicity and anti-neoplasticity through the induction of oxidative stress, mitochondrial dysfunction and apoptosis. *Colloids Surf B Biointerfaces* **2018**, *161*, 111-120, https://doi.org/10.1016/j.colsurfb.2017.10.040.
61. Mortezaee, K.; Najafi, M.; Samadian, H.; Barabadi, H.; Azarnezhad, A.; Ahmadi, A. Redox interactions and genotoxicity of metal-based nanoparticles: A comprehensive review. *Chem Biol Interact* **2019**, *312*, https://doi.org/10.1016/j.cbi.2019.108814.
62. Su, D.M.; Zhang, Q.; Wang, X.; He, P.; Zhu, Y.J.; Zhao, J.; Rennert, O.M.; Su, Y.A. Two types of human malignant melanoma cell lines revealed by expression patterns of mitochondrial and survival-apoptosis genes: implications for malignant melanoma therapy. *Mol Cancer Ther* **2009**, *8*, 1292-1304, https://doi.org/10.1158/1535-7163.MCT-08-1030.
63. Chatterjee, S.J.; Ovadje, P.; Mousa, M.; Hamm, C.; Pandey, S. The efficacy of dandelion root extract in inducing apoptosis in drug-resistant human melanoma cells. *Evid Based Complement Alternat Med* **2011**, *2011*, https://doi.org/10.1155/2011/129045.
64. Ankamwar, B.; Lai, T.C.; Huang, J.H.; Liu, R.S.; Hsiao, M.; Chen, C.H.; Hwu, Y.K. Biocompatibility of Fe3O4 nanoparticles evaluated by in vitro cytotoxicity assays using normal, glia and breast cancer cells. *Nanotechnology* **2010**, *21*, 075102-075110.
65. Gokduman, K.; Gok, A. In vitro investigation of therapeutic potential of bare magnetite (Fe3O4) nanoparticles (≤100 ppm) on hepatocellular carcinoma cells (HepG2). *J Nanosci Nanotechnol* **2020**, *20*, 1391-1400, https://doi.org/10.1166/jnn.2020.17152.
66. Li, L.; Gokduman, K.; Gokaltun, A.; Yarmush, M.L.; Usta, O.B. A microfluidic 3D hepatocyte chip for hepatotoxicity testing of nanoparticles. *Nanomedicine* **2019**, *14*, 2209-2226, https://doi.org/10.2217/nnm-2019-0086.
67. Gokduman, K. Sensitization of cisplatin-resistant ovarian cancer cells by magnetite iron oxide nanoparticles: an in vitro study. *Nanomedicine* **2019**, *14*, 3177-3191, https://doi.org/10.2217/nnm-2019-0126.

6. ACKNOWLEDGEMENTS

This study was supported by the Scientific and Technological Research Council of Turkey (TUBITAK). There is no other relevant affiliation or financial involvement with any organization or entity with a financial interest in or financial conflict with the subject matter or materials discussed in the manuscript apart from those disclosed.